

ORIGINAL RESEARCH

Open Access



Monte Carlo modelling of a compact CZT-based gamma camera with application to ^{177}Lu imaging

Daniel Roth^{1*} , Erik Larsson², Michael Ljungberg¹ and Katarina Sjögren Gleisner¹

*Correspondence:
daniel.roth@med.lu.se

¹ Medical Radiation Physics,
Lund, Lund University, Lund,
Sweden
Full list of author information
is available at the end of the
article

Abstract

Background: Semiconductor gamma-camera systems based on cadmium zinc telluride (CZT) detectors present new challenges due to an energy-response that includes effects of low-energy tailing. In particular, such energy tails produce effects that need to be considered when imaging radionuclides with multiple emissions such as ^{177}Lu . Monte Carlo simulation can be used to investigate the behaviour of such systems and optimise their use, provided that the detector model closely reflects the real physical detector. The aim of this work is to develop a CZT model applicable for simulation of CZT-based gamma cameras.

Methods: The equations describing the charge transport and signal induction are considered in three dimensions and are solved numerically, and the CZT model is then realised by coupling the detector-response to the photon-transport handled by the SIMIND Monte Carlo program. The CZT model is tuned to reproduce experimentally measured energy spectra of a hand-held gamma camera system for multiple radionuclides ($^{99\text{m}}\text{Tc}$, ^{123}I and ^{177}Lu) and parallel-hole collimators (MEGP, LEHR) as well as an uncollimated system.

Results: Overall, the model results agree well with measurements across the range of experimental conditions. The applicability of the model is demonstrated by separating energy spectra into components to investigate the interference of high-energy photons on lower energy-windows, where pronounced effects of low-energy tailing for ^{177}Lu are observed.

Conclusions: The developed model provides understanding of the specifics of the camera response and is expected to be helpful for future optimisation of gamma camera applications.

Keywords: CZT, Handheld gamma camera, Molecular imaging, Monte Carlo

Background

Semiconductor-based gamma cameras utilising cadmium zinc telluride (CZT) are becoming increasingly common in clinical applications [1–7]. Such cameras generally have favourable properties compared to conventional Anger cameras, such as better energy and intrinsic spatial resolution. The detector modules incorporated in CZT

cameras are more compact than the typical photomultiplier tube arrays used in conventional Anger-cameras, and provide useful fields of view (FOVs) equal to the full detector-area. These aspects offer additional advantages and opportunities, as they allow for novel camera designs with efficient measurement geometries (see e.g. [1, 3, 6]). The two major vendors for clinical CZT cameras are GE Healthcare and Spectrum Dynamics Medical, that offer SPECT systems like the Discovery NM530c [1], D-SPECT [2], Discovery 870 CZT [5], Veriton [6] and StarGuide [7]. CZT-based cameras do, however, typically present undesirable spectrum features known as low-energy tails, which result from poor charge carrier transport properties (low mobilities or short lifetimes), particularly for holes, an issue prevalent among compound semiconductors [8]. Special electrode configurations such as pixelated anodes [9] reduce the tails, but do not eliminate them completely. The low-energy tails present problems for imaging of certain radionuclides where high-energy photon emissions contribute to the energy windows set over emissions of lower energy [10, 11].

^{177}Lu is a β^- -emitter used within radionuclide therapy. Its applications include [^{177}Lu]Lu-DOTA-TATE for neuroendocrine tumours [12] and [^{177}Lu]Lu-PSMA for prostate cancer [13, 14]. ^{177}Lu imaging is possible through several photon emissions with suitable energies and yields. The most prominent emissions are 54.6 keV, 55.8 keV, 112.9 keV and 208.4 keV, and the near-indistinguishable combination of the first two emissions is henceforth referred to as 55 keV. For CZT-detectors, the low-energy tailing means that the high-energy photon emissions will contribute to lower energy windows (mainly 113 keV and 55 keV windows). Imaging of ^{177}Lu therefore requires additional considerations compared to radionuclides with simpler, near-monoenergetic, spectra. Implications of low-energy tailing have been studied previously, mainly regarding dual-isotope acquisitions of $^{99\text{m}}\text{Tc}+^{201}\text{Tl}$ and $^{99\text{m}}\text{Tc}+^{123}\text{I}$ [10, 15–18].

Monte Carlo simulation is a tool used to investigate the performance and improve the understanding of detector systems. A major advantage is that effects that are difficult to investigate by experimental measurements can be readily isolated and studied. Complete modelling of a detector measurement requires that a number of processes are addressed, including the radiation emission and transport, the interactions in the detector, the generation of electrical output-signals from the detector and the post-processing of these signals. These processes can be modelled at different levels of detail, with a degree of complexity that depends on the targeted detector system and its application [19]. Monte Carlo modelling of scintillation-based gamma cameras is well-established, whereas the modelling of their semiconductor-based counterparts is a newer field in which more detailed considerations of the signal-generation process are required. For Anger-type scintillation-camera models it may suffice with a simplified scintillation light collection model with a fixed position-independent collection fraction, whereas for semiconductor-based detectors the response to the motions of the created electron-hole pairs is position-dependent and needs to be considered. This position dependence can be modelled with different degree of complexity, ranging from simpler one-dimensional approximations [20] to comprehensive three-dimensional models [21], or somewhere in-between the two [22, 23].

The number of Monte Carlo programs that readily includes modelling of CZT imaging is currently limited, and those that exist sometimes rely on simplified analytical

expressions whose validity may affect the accuracy. In addition, the use of CZT signal generation models requires knowledge of parameters and material properties that may be impractical to measure directly by end users of CZT cameras. Consequently, reaching the point where simulations agree sufficiently well with measurements may be challenging. In particular, our initial attempts with a simplified CZT model, presented in [23], for a small hand-held gamma camera [3, 11] gave poor agreements when evaluated across multiple parallel-hole collimators and radionuclides. Especially, accurate simulation of ^{177}Lu with its three energy peaks has proved to be challenging, possibly due to the validity of the assumptions and approximations made by the employed model.

Thus, the aim of this work was to develop a CZT model for imaging and spectroscopy, combine it with the SIMIND Monte Carlo program [24] for photon transport, and investigate a practical method of tuning it against experimental measurements with the hand-held camera. This is a system centred around a single CZT-module [25], whose specifications are identical or similar to modules found in full-size gamma cameras (e.g. [1, 2, 4, 5]), and the developed model should therefore be relevant for such systems as well (personal communication, Aharon Peretz, General Electric, retired).

Materials and methods

Charge transport and signal induction

For CZT-based semiconductor detectors, the strong interaction-position-dependence of the detector signal can be calculated with the Shockley–Ramo theorem [26–28], as outlined in detail in Additional file 1: Appendix A. The detector response can be calculated from the equations

$$\nabla^2\varphi = \frac{\rho}{\varepsilon}, \quad (1)$$

$$\nabla^2\varphi_k = 0, \quad (2)$$

$$\frac{\partial x}{\partial t} = \pm \nabla \cdot (\mu_x x \nabla \varphi) + \nabla \cdot (D_x \nabla x) + G_x - R_x, \quad (3)$$

$$\Delta Q_{x,k}(t) = q \cdot \int_0^t \int_{\mathbf{r} \in \Omega} x(\mathbf{r}, t') \cdot \mu_x \cdot \nabla \varphi(\mathbf{r}) \cdot \nabla \varphi_k(\mathbf{r}) d\Omega dt'. \quad (4)$$

Equation 1 is Gauss's law, which is solved for the electric potential φ in the detector crystal, ρ is the charge density and ε is the permittivity of the detector crystal [29, 30].

Equation 2 gives the so-called weighting potential φ_k for electrode k that is attached to the detector crystal.

Equation 3 describes the motion of a cloud of excess charge carriers [19, 30, 31], which for semiconductors can represent electrons ($x = n$) or holes ($x = p$). The sign of the first term is negative for electrons and positive for holes, μ_x is the charge carrier mobility, D_x is the diffusion constant [32], and G_x and R_x express the creation of new charges and recombination of existing charges, respectively. Charge recombination can be described as $R_x = x/\tau_x$, where τ_x is the charge carrier lifetime. A typical generation term in the context of radiation interactions is the creation of a single point-like charge generated

at an arbitrary point \mathbf{r}_0 at time $t = 0$; $G_x = \delta(|\mathbf{r} - \mathbf{r}_0|) \cdot \delta(t)$, where $\delta(\cdot)$ is the Dirac delta function.

Equation 4 is the Shockley–Ramo theorem, and gives the charge ΔQ that is induced on electrode k due to the motion of a charge cloud $x(\mathbf{r}, t)$, where Ω is the crystal volume [19, 22, 30, 31].

The induced charge can be considered as a function of the integration time t , and the point \mathbf{r}_0 where the charge was initially created, i.e. $\Delta Q_{x,k}(t) = \Delta Q_{x,k}(\mathbf{r}_0, t)$. The charge induction efficiency (CIE) η is a quantity that summarises the detector response as function of interaction position, and is defined as $\eta_{x,k}(\mathbf{r}_0, t) = Q_{x,k}(\mathbf{r}_0, t)/|q|$.

Calculation of $x(\mathbf{r}, t)$ and $\eta_{x,k}(\mathbf{r}_0, t)$ for a large number of starting positions \mathbf{r}_0 directly using Eqs. 3 and 4 is computationally expensive. A more efficient method for computing η is to use an adjoint method [19, 31], which introduces the equation

$$\frac{\partial x^+}{\partial t} = \mp \mu_x \nabla \varphi \cdot \nabla x^+ + \nabla \cdot (D_x \nabla x^+) + G_x^+ - x^+/\tau_x, \quad (5)$$

where the sign of the first term is positive for electrons and negative for holes. With G_x^+ defined as $G_x^+ = \mu_x \nabla \varphi \cdot \nabla \varphi_k$ it can be shown that $x^+(\mathbf{r}, t) = \eta_{x,k}(\mathbf{r}, t)$ [19, 31], meaning that $\eta_{x,k}(\mathbf{r}, t)$ can be determined for all starting positions by solving Eq. 5 once.

The hand-held camera

The camera used was a CrystalCam hand-held gamma camera (Crystal Photonics GmbH, Berlin, Germany). The primary application for the instrument is sentinel lymph node localisation with ^{99m}Tc , but other applications have been evaluated as well [3, 11]. The camera uses a single OMS40G256 CZT module (Orbotech Medical Solutions Ltd., Israel, now GE Healthcare) for imaging, with a crystal of dimensions $39 \times 39 \times 5 \text{ mm}^3$. One side of the crystal is covered by a continuous cathode, and the opposing side by a 16×16 array of anode elements with a 2.46 mm pitch and a contact pad size of $1.86 \times 1.86 \text{ mm}^2$. A 600 V potential is applied over the crystal, and the electrode properties are specified as ohmic. Further descriptions of similar modules are given by Vadawale et al. [33] and Kotoch et al. [25].

Collimators used were low energy high resolution (LEHR) and medium energy general purpose (MEGP), and also an open-field cover (OPEN) that has an air-cavity in place of collimating material. The collimators have holes matched one-to-one with the anodes of the detector. Collimator specifications are given in Table 1.

The camera can be used in low-energy mode, covering an energy interval of approximately 40 to 250 keV and high-energy mode, covering 40 to 1250 keV. Only the low-energy mode was used, as the high-energy mode exhibits greater inhomogeneities and is less suitable for imaging. The acquired data were stored in a table of spectra, stating for

Table 1 Collimator dimensions

Name	Hole length	Wall thickness	Hole width	Material	Hole shape
LEHR	22.6	0.23	2.23	Lead	Square
MEGP	11.5	0.96	1.50	Lead	Circular

All values are given in mm. Table adapted from Roth et al. [11]

each anode element the number of counts as function of energy according to the manufacturer's energy calibration, including equally spaced energy bins between 0 keV and 250 keV with a bin width of 0.1 keV.

Experimental measurements

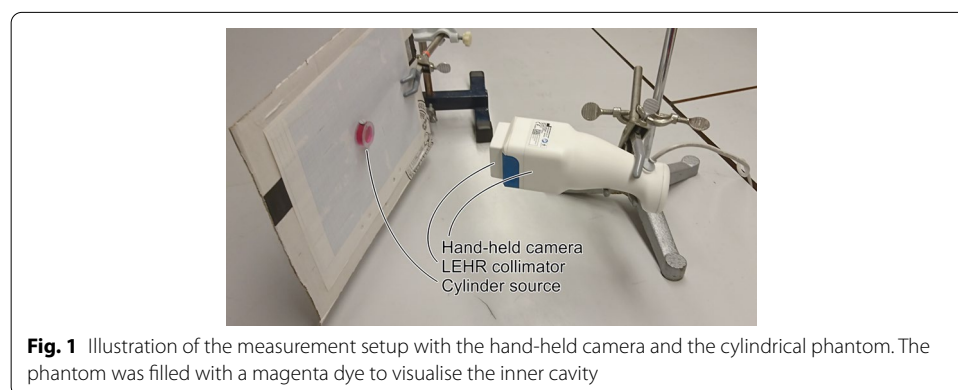
Reference measurements were made to tune the detector model. A resealable phantom was used, consisting of a cylindrical cavity (20 mm diameter, 8 mm height) with PMMA walls (1 mm top and bottom thickness, 5 mm radial thickness) [11]. Spectra were acquired with the following radionuclides and collimators: ^{177}Lu (MEGP, LEHR), $^{99\text{m}}\text{Tc}$ (MEGP, LEHR, OPEN) and ^{123}I (MEGP, LEHR, OPEN). A traceable Secondary Standard Dose Calibrator (Southern Scientific, Henfield, United Kingdom) was used to quantify the activity added to the phantom. Measurements were made with the phantom in air to minimise scatter and backscatter, with source-collimator distances of between 25 mm and 150 mm. Figure 1 illustrates the measurement setup.

The model was further evaluated by measurements of the system sensitivity as a function of distance for ^{177}Lu with the MEGP and LEHR collimators. The setup for sensitivity measurements were similar to that of the reference measurements, using source-collimator distances from 0 mm up to 100 mm (MEGP) and 130 mm (LEHR). Energy windows were positioned over 55 keV (49.7 keV to 59.7 keV), 113 keV (100.5 keV to 120.8 keV) and 208 keV (193.8 keV to 216.7 keV), and the total count rates across the full FOV were recorded. For the measured sensitivity, a function was fitted following $c_0 + c_1 \cdot e^{-c_2 \cdot d}$, where d is the source-collimator distance [34].

CIE map calculation

A procedure for calculating CIE maps was implemented in Python using arrays, sparse matrices and linear equation solvers from the NumPy [35] and SciPy [36] packages. The procedure considered a rectangular crystal volume in a Cartesian coordinate system oriented consistently with the convention used by SIMIND. The source-facing side of the crystal was fully covered by a cathode. The opposing side was covered by an array of rectangular anode elements, and the signal generation for one selected anode in this array was considered.

Finite difference approaches [37] were used to numerically estimate the solutions to differential equations 1, 2 and 5. For boundary-value problems (Eqs. 1 and 2), this



yielded systems of linear equations which were solved using the loose generalised minimum residual algorithm [38].

The boundary conditions implemented for the differential equations were as follows: For the electric potential (φ), a specified potential difference (600 V) was applied between the anodes and the cathode. The weighting potential (φ_k) was, by definition, calculated with one selected electrode (electrode k) held at a potential of unity and all other electrodes at zero. For charge transport ($x \in \{n, p, n^+, p^+\}$), the condition $x = 0$ was applied on ohmic surfaces and $\nabla x \cdot \hat{n} = 0$ was applied on insulating surfaces, where \hat{n} is the surface normal [19].

For the inter-anode gaps, the camera’s technical description did not provide sufficient basis for a model implementation of the electrical and weighting potentials. In addition, it was not clear whether the signal contribution from holes was entirely negligible or not. Because of this lack of information, a number of alternative boundary conditions and configurations were implemented (Table 2) and tested as part of the model tuning (“Model tuning” section).

For the electric potential (φ), alternative A1 represented the commonly used assumption of a uniform electric field throughout the crystal [20, 22, 23, 39]. Alternative A2 instead assumed that the electric field lines start and end on electrodes, as expected for ideal dielectric materials [40, 41]. For A2, Eq. 1 was solved with charge density assumed negligible [42]. For imperfect materials with conducting surfaces, a fraction of the field lines may terminate in the inter-anode gaps [40–42], as emulated by alternative A3.

For the weighting potential (φ_k) a transition from unity to zero must occur in the gaps between the selected anode and its neighbours. A boundary condition involving the gradient and the surface normal is commonly applied [31, 39, 43, 44], represented by alternative B1. The inverse-distance weighting [45] method (alternative B2) has not been used previously, and was introduced to obtain way to parametrise and adjust the steepness of the lateral sides of the weighting potential and CIE. Additionally, a scale factor was introduced for alternative B2 to force the weighting potential to reach zero at the edge of the neighbouring anode or at some position within the gap, thus allowing for

Table 2 Configurations and boundary conditions considered for the CIE calculation procedure

Component (equation number)	Alternative	Configuration	Effective number of tunable parameters ^b
Electric potential	(1) A1	Uniform electric field	0
	(1) A2 ^{a,c}	$\nabla\varphi \cdot \hat{n} = 0$	0
	(1) A3	Weighted average of the results from A1 and A2	1
Weighting potential	(2) B1 ^a	$\nabla\varphi_k \cdot \hat{n} = 0$	0
	(2) B2	Inverse-distance weighted transition	2
Signal generation	(5) C1	Electrons only	2
	(5) C2	Electrons and holes	3

^aBoundary condition applied on inter-anode gaps.

^bParameters are listed in Additional file 1: Appendix E.

^cAlternative A2 was not used on its own and is only defined here to clarify the definition of A3

adjustment of the "width" of the anode's sensitive area. Further details on alternative B2 are given in Additional file 1: Appendix B.

Signal generation from electrons only (C1) or both electrons and holes (C2) were considered. Equation 5 was implemented using a first-order upwinding scheme. The signal integration time was assumed to be long compared to the collection times and the lifetimes of the charge carriers, and the boundary-value problems arising from setting $\partial x^+ / \partial t = 0$ were solved rather than integrating Eq. 5 forward in time.

Due to the periodic pattern of the anode elements, a number of calculated quantities were expected to be symmetric [40, 46, 47]. In particular, this was expected for the electric potential, the weighting potential and the CIE for anode elements near the centre of the detector. For each established plane of symmetry, only one side was considered when solving the equations, and all gradients across were set to zero.

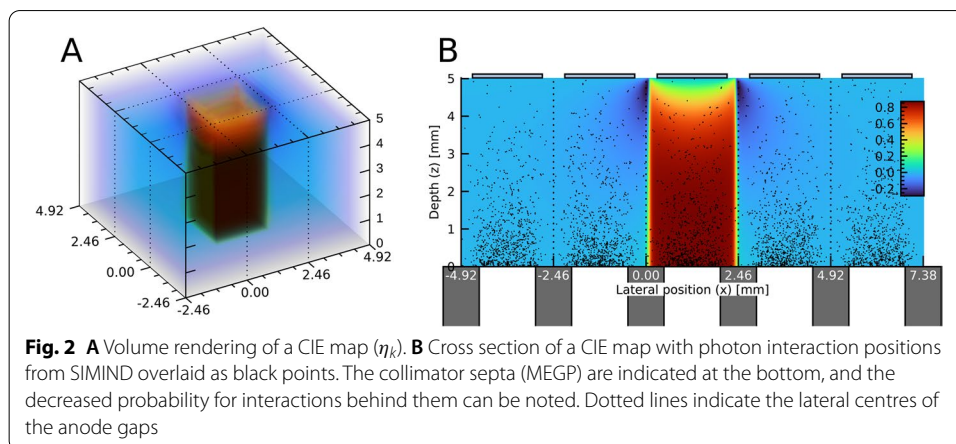
To reduce the computational burden and get manageable calculation times, a compromise was necessary between the extent of the crystal region considered and the spatial discretisation step size. Thus, a 5×5 anode element neighbourhood centred around the selected anode was considered instead of the whole crystal, giving a step size of $20 \mu\text{m}$.

Once all calculations were complete, the CIE map was written to a binary file for later use in the full detector model, including the CIE array, the coordinates associated with the array elements and a selection of parameter values (μ_x, τ_x etc.) for book-keeping.

For consistency control, a CIE map was also calculated without charge diffusion in a parallel-plate geometry (single anode and cathode each covering the entire sides). For this geometry, the electric and weighting fields are uniform. With these conditions, the resulting CIE had a depth-dependence consistent with the Hecht-equation [48].

Monte Carlo simulation of photon interactions

The SIMIND Monte Carlo program [24] was used to generate sets of realistic photon interactions in the detector crystal. This was made for each of the physical measurements ("Experimental measurements" section). The collimators were simulated with full consideration of the collimator hole geometry and holes were aligned one-to-one with the detector anodes, to properly model the decreased likelihood of interactions above the gaps between the anodes. This collimator effect is visible in Fig. 2. Each photon interaction in the detector crystal was logged in a listmode format, including information



about the interaction type (photoelectric absorption, Compton scatter, elastic scatter), interaction coordinates, deposited energy and variance-reduced photon weight [49]. The events originating from different photon histories were recorded as separate entries in the listmode file.

Full detector model

A detector model mimicking the hand-held camera system was implemented in IDL (Interactive Data Language, Harris Geospatial Solutions Inc.). The basic building blocks were individual anode elements, which processed events separately from one-another. A CIE map (η_k) was associated to each element, and was defined according to

$$\eta_k(\mathbf{r}) = \eta_{\text{joint}}(\mathbf{r} + \mathbf{r}_k - \mathbf{r}_{\text{joint}}), \quad (6)$$

where η_{joint} was generated using the procedure in “CIE map calculation” section. This joint CIE map, implemented in the form of a discrete three-dimensional array, was calculated for a central anode element ($\mathbf{r}_k = \mathbf{r}_{\text{joint}}$). The associated maps for all other anode elements ($\mathbf{r}_k \neq \mathbf{r}_{\text{joint}}$) were determined by applying suitable translations (Eq. 6). The full detector model was obtained by creating a 16×16 array of individual anode elements.

The model used the listmode files generated by SIMIND as input. For each photon history H , the total response $E_{\text{out},k}$ for each anode element k was calculated according to

$$E_{\text{out},k} = \sum_{i \in H} \eta_k(\mathbf{r}_i) \cdot E_i, \quad (7)$$

where i denotes an individual photon interaction event for which the energy E_i is deposited at a point \mathbf{r}_i . Tri-linear interpolation within the CIE array was used to evaluate $\eta_k(\mathbf{r}_i)$. This coupling between a calculated CIE map and interactions from SIMIND is illustrated in Fig. 2.

Following Eq. 7, each photon history yielded 256 separate energy-responses $E_{\text{out},k}$ (one per anode element). Due to photon scattering and charge sharing, the response was not limited to a single anode [50]. Generally one or a few anodes produced substantially higher values of $E_{\text{out},k}$ than others. As the technical specifications of the detector module indicated that only one anode registers a count per impinging photon, a post-processing step was included in which the anode with the largest value of E_{out} was assigned to win the photon history, while $E_{\text{out},k}$ from all other anodes were discarded. The signal from the winning anode was used to record a count (scaled by the photon weight) in the energy spectrum. These initial spectra did not incorporate any energy resolution effects beyond the photopeak widening caused by the low-energy tails. Furthermore, as η_k had values below unity ($\eta_k < 0.9$ in Fig. 2), the photopeaks tended to shift downwards. To take these factors into account, two subsequent steps were applied. In the first step, the spectrum was re-sampled according to a linear energy-calibration:

$$E_{\text{corr}} = a_0 + a_1 \cdot E_{\text{init}}, \quad (8)$$

where E_{init} was the energies of the uncalibrated spectrum, and E_{corr} were the new energies calculated such that the photopeaks were aligned with the corresponding photon emission energies. The second step aimed at mimicking additional energy resolution

effects by applying a Gaussian smoothing with an energy-dependent full width at half maximum (FWHM), as given by:

$$\text{FWHM}(E) = b_0 + b_1 \cdot E. \quad (9)$$

Application of Eq. 8 mimics the calibration of energy-versus-channel number used by the camera manufacturer [3]. The linear function for the FWHM (Eq. 9) was used based on the findings in Roth et al. [11].

Because the application of the energy resolution had a small effect on the peak positions, an iterative procedure was developed in which the parameters of the energy calibration (Eq. 8) were solved for given values of the energy resolution parameters (Eq. 9). Thus, the parameters a_0 , and a_1 were determined such that the photopeaks would be correctly placed after the energy resolution step (for details, see Additional file 1: Appendix C).

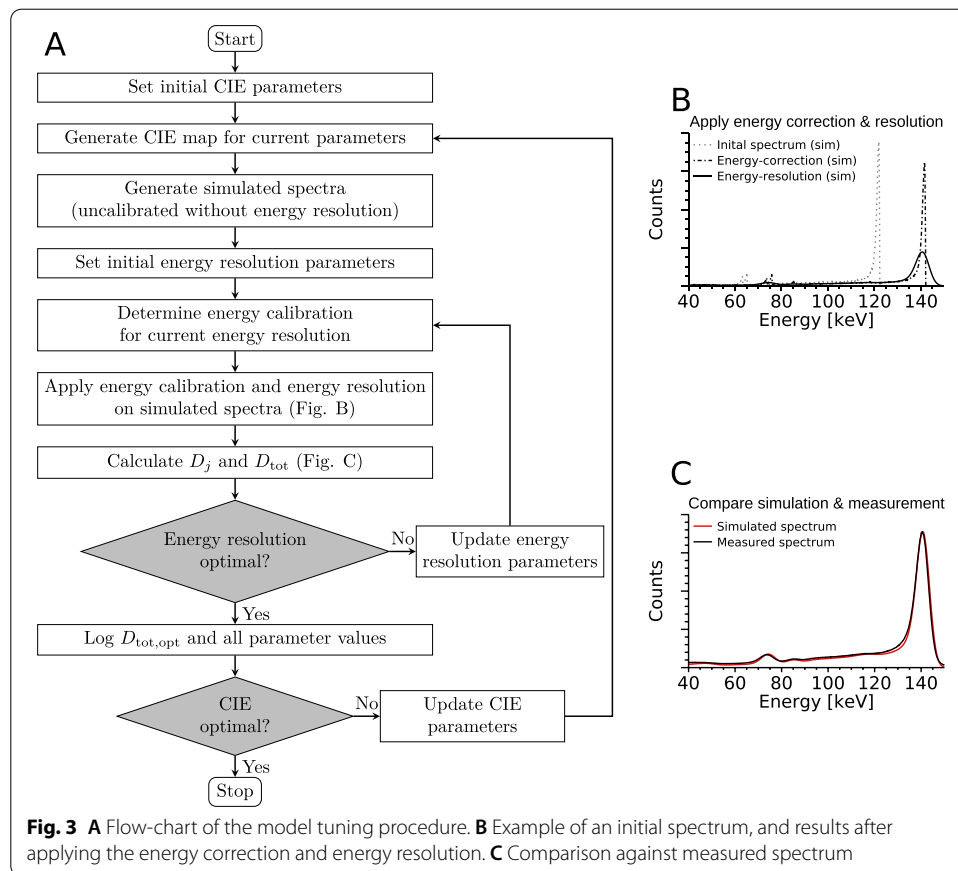
Energy spectra were recorded for individual anode elements in a format identical to that of the camera (“[The hand-held camera](#)” section). This format allowed spectra to be formed by adding the spectra from selected anode elements. With the anode element arrangement known, image formation was achieved by integrating all counts within a given energy-window for each individual anode-spectrum. In addition, information provided in the simulation listmode files allowed the spectra to be divided into components based on the photon classification (primary, scatter, penetration etc.) and original emission energy.

Model tuning

“[The hand-held camera](#)” section lists specifications and parameters known for the camera and its detector module. Beyond these, other parameters such as charge mobilities, charge lifetimes, and the shapes of the electric and weighting potentials, were not known with precision. The crystal properties are known to vary throughout manufactured CZT ingots [51], and a relatively wide range of mobilities and lifetimes for electrons and holes has been reported in the literature [8, 30, 44, 52–54]. A further complication was that the features of the CIE map (η_{joint}) and the energy resolution were not independent of each other, since the magnitude of the low-energy tails were governed by the CIE map, and in turn, these tails contributed to the energy resolution. Consequently, experimentally determined energy resolution functions [11] were not directly applicable.

Because of these factors, tuning of the parameter values and boundary conditions was required, with the goal of obtaining a detector model capable of replicating the experimental measurements as closely as possible. To take the large amount of experimental measurements (“[Experimental measurements](#)” section) and adjustable parameters into account simultaneously, the parameter tuning was performed as an automated procedure, illustrated in Fig. 3.

The different CIE settings listed in Table 2 were combined, and together yielded eight basic CIE configurations (Additional file 1: Appendix D). The parameter tuning procedure was executed separately for each of these configurations. In each run, the values of the configuration-associated parameters (Additional file 1: Appendix E) were optimised (outer loop in Fig. 3). Given a set of parameter values, a CIE map (η_{joint}) was generated. For each radionuclide-collimator combination, the Monte Carlo simulated photon



interactions were processed with this CIE map to form an initial spectrum (Eq. 7), the energy calibration parameters were determined, and the energy calibration and resolution applied. The energy resolution parameters were optimised separately from the CIE parameters (inner loop in Fig. 3), as the generation of a new CIE map was by far the most time-consuming step. The same energy calibration was used for all simulated spectra, and was determined using the simulation of ^{177}Lu and MEGP. To enable direct comparison of measured and simulated spectra, energy calibration was also made for the measured spectra to ensure consistent photopeak positioning, which otherwise varied slightly depending on the detector temperature at measurement [11, 33]. The simulated spectra were scaled to correspond to the same activity and acquisition time as the corresponding measured spectra, and the level of agreement was determined according to

$$D_j = \frac{\sum_{E \in W_j} (f_j \cdot S_{\text{sim},j}(E) - S_{\text{ref},j}(E))^2}{\left(\sum_{E \in W_j} S_{\text{ref},j}(E)\right)^2}, \quad (10)$$

where j denotes one pair of simulated and measured spectra ($S_{\text{sim},j}$ and $S_{\text{ref},j}$). The energy interval W_j was set to cover the total range of the radionuclide emissions and the operational range of the detector. The factor f_j was introduced as a free parameter for simulations without a collimator (open-field) for which the system response was very sensitive to the exact source-collimator distance used at measurement. For simulations

that included a collimator, f_j was set to unity. Since anode elements near the edges of the detector crystal can theoretically have a different, inferior, response compared to central anodes [39], $S_{\text{sim},j}$ and $S_{\text{ref},j}$ were defined as the sum of the spectra from the central 14×14 anode elements.

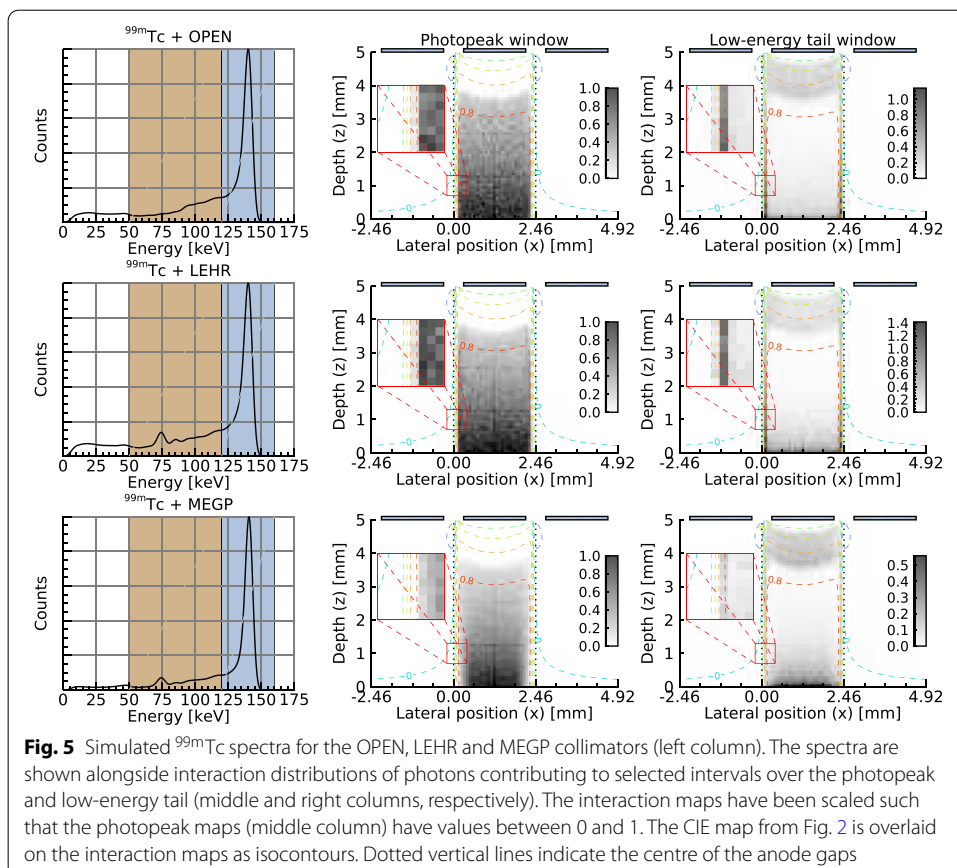
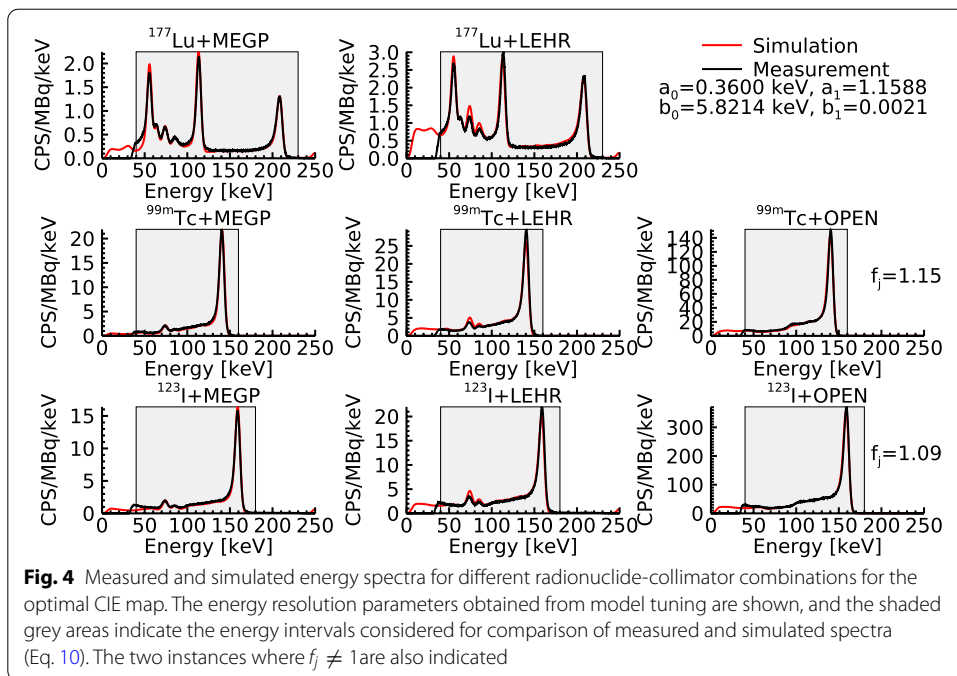
The total level of agreement D_{tot} across all spectrum pairs was calculated as $D_{\text{tot}} = \sum_j D_j$. The value of D_{tot} depended on the CIE map and its parameter values, as well as the energy resolution parameters (Eq. 9). The energy resolution parameters that yielded the lowest D_{tot} value ($D_{\text{tot,opt}}$) for a given CIE map were determined using a downhill simplex method [55], with initial estimates $b_0 = 5.64$ keV and $b_1 = 0.00751$ [11] (inner loop in Fig. 3). The optimal CIE map was then determined by a second simplex optimisation (outer loop in Fig. 3), in which the $D_{\text{tot,opt}}$ value was considered as a function of the parameters of the CIE map. The optimal CIE map, with associated optimal energy calibration and energy resolution parameters, was thus obtained as the one yielding the best agreement (lowest $D_{\text{tot,opt}}$).

Results

The optimal CIE map was obtained using configuration A1-B2-C1 (Table 2), i.e. using a uniform electric field, a weighting potential based on the inverse-distance-weighted transition and signal generation from electrons only. This CIE map is visualised in Fig. 2, and the associated weighting potential is shown in Additional file 1: Figure S1 (Appendix A). Results below are given for this optimal CIE map, with its optimised energy resolution parameters. A summary of the levels of agreement obtained for all configurations is provided in Additional file 1: Appendix D, and associated initial and optimal parameter values are given in Additional file 1: Appendix E.

Figure 4 shows measured and simulated energy spectra for the different radionuclide-collimator combinations used in the model tuning. Generally there is a good agreement between simulation and measurement, with small remaining deviations for x-ray peaks at lower energies for the LEHR collimator.

Figure 5 shows simulated $^{99\text{m}}\text{Tc}$ -spectra for the OPEN, LEHR and MEGP collimators. The spatial distribution of photon interaction events in the detector crystal contributing to selected spectral intervals (photopeak and low-energy tail) are illustrated besides each spectrum. All or most of the events that contribute to the photopeak occur within the relatively flat region of the CIE map ($\eta_k \simeq 0.8$ in Fig. 2), with a sharp decrease in event density where the CIE-value drops below approximately 0.7. The density of events that contribute to the photopeak decreases with increasing crystal depth due to photon attenuation. For the low-energy tail there is a contributing region near the anode, which results from the poor transport properties of holes and the small depth dependence that is still present for small-pixel devices [9]. There is also contribution from a region near the cathode, likely due to Compton and x-ray escape events as well as scattered photons and x-rays from the collimator, when present. In addition, there is contribution from regions near the lateral edges of the CIE, attributed to charge diffusion and charge sharing between neighbouring anodes [50]. The MEGP collimator shows few events in this region due to the thicker collimator septa, and as a result the low-energy tail for the MEGP collimator is lower than those of the other collimators. The remaining tail for the MEGP collimator is mainly caused by the depth-dependence of the detector.



Further model validations are shown in Fig. 6, which includes energy spectra, images and image profiles for ^{177}Lu with the LEHR and MEGP collimators. The ^{177}Lu measurements are the same as in Fig. 4, and the source-collimator distances are 48 mm and 25 mm for the LEHR and MEGP collimator, respectively. The simulated spectra are separated into sub-components that reflect the contribution from the different emission energies of ^{177}Lu . The separation makes the interference of 208 keV photons at lower energies evident, which is more pronounced for LEHR than for MEGP. The model's capability of producing images is also demonstrated, replicating the phantom used for measurement and using an energy window positioned over the 113 keV peak (100.5 to 120.8 keV). The profiles enable comparison of the imaging characteristics between the simulations and measurements, where a uniformity correction has been applied for measured data [11]. To aid the profile comparison, the simulated images have been scaled to the same total number of counts as for the measurements, due to small differences in system sensitivities. Slight discrepancies between measured and simulated image profiles are obtained due to difficulties of exactly replicating the position of the source in relation to the pixelated detector array and the source-collimator distance, but overall the profiles agree well.

Figure 7 shows results of the system sensitivity for ^{177}Lu as a function of the source-collimator distance, obtained from measurements and simulations for the LEHR and MEGP collimators. The simulated sensitivity is further separated into different sub-components, including collimated primary, phantom scatter, collimator penetration, collimator scatter and collimator x-rays, where the term primary denotes photons that pass un-scattered from the site of decay to the detection point

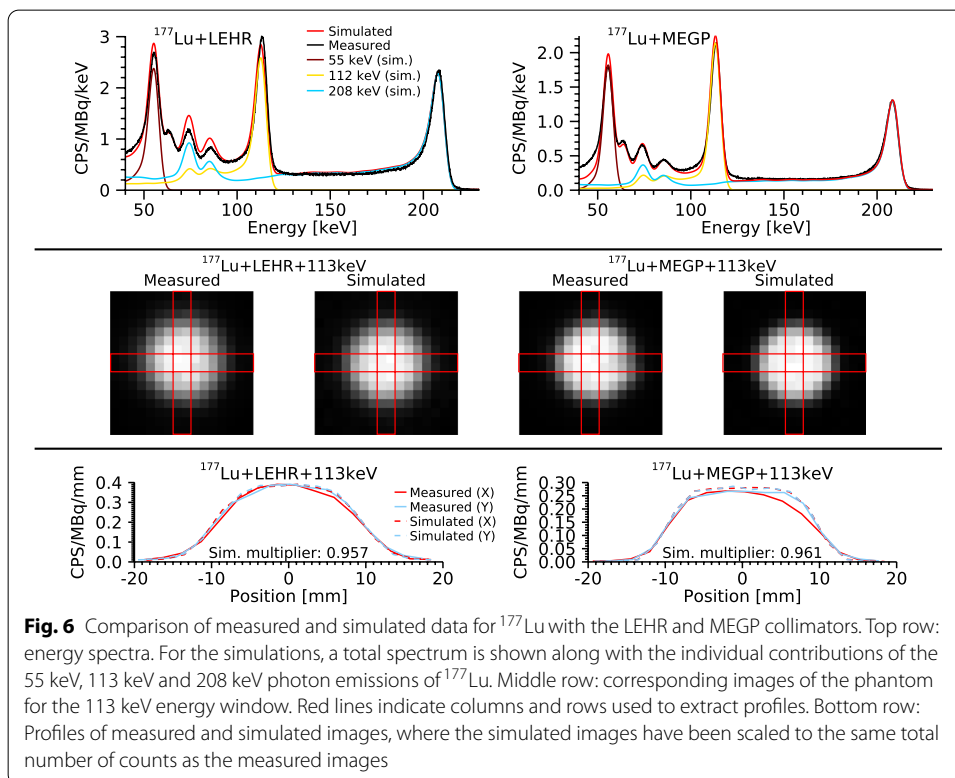
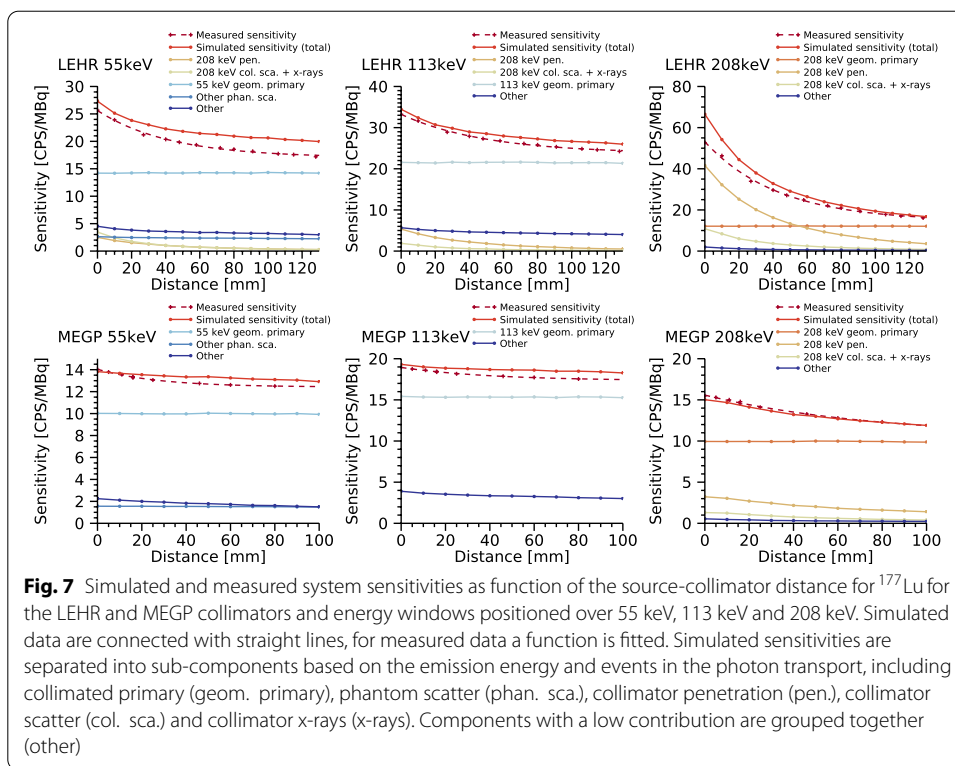


Fig. 6 Comparison of measured and simulated data for ^{177}Lu with the LEHR and MEGP collimators. Top row: energy spectra. For the simulations, a total spectrum is shown along with the individual contributions of the 55 keV, 113 keV and 208 keV photon emissions of ^{177}Lu . Middle row: corresponding images of the phantom for the 113 keV energy window. Red lines indicate columns and rows used to extract profiles. Bottom row: Profiles of measured and simulated images, where the simulated images have been scaled to the same total number of counts as the measured images



in the crystal, and the term scatter refers to photons that have undergone Compton or Rayleigh scattering prior to detection. The system sensitivity generally decreases as a function of the source-collimator distance, irrespective of the energy window or collimator used. The simulations elucidate the cause of this behaviour: while the geometric primary component has a stationary response, the collimator penetration of primary 208 keV photons exhibits a pronounced distance dependence. This mainly affects the 208 keV window, but energy windows set at lower energies are also affected due to the low-energy tails associated with the detector. Likewise, x-rays from the collimator and 208 keV photon scatter in the collimator septa contribute to the distance-dependence. Quantitatively, the best overall agreements between simulated and measured data are obtained for the MEGP collimator and 208 keV energy window, with an average deviation obtained of 2%. The poorest overall agreement is obtained for the LEHR collimator and the 55 keV window, with an average deviation of 12%. For this energy window, errors are associated with the lower-level energy cutoff in the measured data for which exact information was not available, and also a high dependency on the modelling of the low-energy tails from both the 208 keV and the 113 keV peaks. Thus, modelling of the 55 keV peak is challenging.

Discussion

Modelling of CZT-based gamma cameras requires more detailed considerations of the information-carrier transport and signal generation, as compared to scintillation-based detectors. To date, different models have been presented (e.g. [20–23]), with different assumptions and approximations made. The applicability of the approximations depends on the experimental conditions for which the model is evaluated, including factors such as the collimators and radionuclides used and the energy intervals considered. The aim of this work was to develop a model for charge transport and signal generation that is applicable across different radionuclides and collimators, and to combine this model with the SIMIND Monte Carlo code for modelling of photon transport. In particular we focused on the radionuclide ^{177}Lu that was found to be the most challenging among the radionuclides evaluated, owing to the three photopeaks combined with the low-energy tails characteristic of CZT detectors. The model was tuned and evaluated using the hand-held CZT camera system, for which the CZT module is identical or equivalent to those included in full-size gamma cameras (personal communication, Aharon Peretz, General Electric, retired). Figure 4 demonstrates the performance of the model, which is stable across the radionuclides and collimators tested. Overall, the obtained results agree well with measurements, allowing for simulation studies of different properties of CZT-based camera systems.

A number of assumptions and approximations have been made in order to reduce the model complexity and deal with unknown camera characteristics. As a consequence the model represents an idealised detector with a uniform response, since all anode elements are assigned identical CIE arrays and energy resolution parameters. In characterisation studies, CZT modules have been found to have a varying response between anode elements [11, 25, 33]. The CIE array and energy resolution determined as part of the model tuning thus represent an average of the detector characteristics, and differences between simulations and measurements may occur if only a few anodes are irradiated and these anodes deviate from the average. In addition, it has been reported that anode elements along the edges of the CZT module can have a different response than central anodes [39]. This effect is less relevant for the hand-held camera, as it only incorporates a single CZT module whose edge elements have limited contribution as long as the object is placed in the central FOV. Edge effects are probably more relevant for larger cameras that incorporate tiles of detector modules.

In the model tuning, the best agreement was obtained using the inverse-distance-weighted approach to define the weighting potential (Additional file 1: Appendix B). This approach is not justified by any physical processes, and should mainly be seen as a modelling tool. The reason that this approach yielded the best agreement is possibly linked to the simplifying assumptions regarding the electric potential, in particular that space charge is assumed negligible (ρ in Eq. 1) and that no special consideration is made for the near-surface crystal-properties. Experiments by others indicate that such effects can influence the anode signals, but would require additional model detail [41, 42]. In our model the end results of any such effects would probably be emulated by the electric potential and weighting potential. The more physically correct approaches are those that allow for non-uniform electric fields and apply gradient-based boundary conditions for the weighting potential, i.e. alternatives A3 and B1. However, these alternatives do not

cover all electrical potentials and weighting potentials that theoretically exist, which can explain the poorer results for e.g. configuration A3-B1-C1 (Additional file 1: Appendix D).

Signal-contribution from holes has been considered, which mainly affects the CIE-value close to the anode. By including holes, the CIE goes towards a non-zero value near the selected anode [56], while without holes it goes towards zero (Fig. 2). These two alternatives have a relatively low impact on D_{tot} (Additional file 1: Appendix D), and the best agreement was obtained by considering electrons only. This can be physically motivated by the low mobility and lifetime for holes, and is common in the literature [22, 30, 31, 39, 44, 50]. It should be noted that the measured spectra have a low-energy cutoff of approximately 40 keV, and it is possible that the contribution from holes would be more relevant for energies below this cutoff.

The SIMIND Monte Carlo program only handles the transport of photons. Rather than modelling the transport of secondary high-energy electrons, each photon interaction in the detector crystal has been assumed to yield a point-like charge cloud (Eq. 7). The maximum electron range is estimated to be approximately 100 μm , corresponding to 200 keV [57], which is in the same order as the 20 μm spatial step size used in the charge transport calculations. Since the CIE map does not appreciably change over these distances (Fig. 2), the handling of the high-energy electrons is expected to have a limited impact on the results.

The model currently uses the values of $E_{\text{out},k}$ (Eq. 7) to determine the winning anode for each photon history, and then applies the energy calibration and energy resolution. In practice it is reasonable to assume that the selection of a winning anode involves time-dependent anode-signals and a signal threshold, for which a more detailed approach would require a time-dependent CIE ($\eta_k(\mathbf{r}, t)$) as well as timestamps for each photon interaction event. Furthermore, in practice signal noise is present at this stage, yielding randomness in the anode selection. These effects are, however, expected to have a minor influence and appear mainly for lower energies, as the induced charge must be shared near-equally between at least two anodes. A final aspect is that the currently applied energy resolution is only a function of the detector out-signal. A more detailed model would attribute the energy resolution to specific effects, including fluctuations in the number of created charges, in the number of trapped charges and electronic noise [54]. Quantification of these components would, however, likely require specialised equipment and disassembly of the camera system, and the current approximation works well for our applications.

Equations 7–9 assume that the readout-electronics have an idealised response, corresponding to a multichannel analyzer (MCA) whose channel number is linearly proportional to $E_{\text{out},k}$. In effect, this assumes that the photon transport (modelled by SIMIND) and the charge transport effects (incorporated in η_k) are the major factors affecting the detectors spectral response, while effects from the preamplifier, shaping amplifier and MCA (e.g. ballistic deficit [29]) are minor and are only included indirectly by the applied energy resolution.

Model tuning and evaluation have, as far as possible, been made based on the unaltered count levels of the measurements and the model (e.g. Eq. 10 and Figs. 4 and 7). The capability of SIMIND to replicate the system sensitivity of Anger-based cameras

is already well-established (see e.g. Gustafsson et al. [58]). Some deviations between simulated and measured sensitivities are, however, expected, and include uncertainties related to the dose calibrator measurements, photon-yields and attenuation coefficients [58], as well as imperfectly replicated measurement geometries.

Results in Fig. 7 generally show good agreement between simulated and measured system sensitivities. Some remaining differences are, however, obtained, where the measured sensitivity is lower than the simulated one. This can in part be attributed to the small FOV of the camera, which increases the impact of measurement setup errors. For the simulations, the source is always perfectly aligned with the FOV centre, whereas any off-centre positioning in the measurements can lead to a loss of counts. Especially for the LEHR collimator and 208 keV there is an increasing overestimation as the source approaches the camera, which indicates an erroneously high penetration fraction. Given the good agreements obtained for the MEGP collimator for the same photon energy and the thin septa of the LEHR collimator, these results indicate that there may be an error in the technical specifications of the LEHR collimator, and adjustment of the septal thickness may be motivated. For the 113 keV and 55 keV windows the deviations are more likely attributable to the CZT model, as the contribution from septal penetration becomes smaller and the tailing-effects from higher-energy photons more pronounced.

Figure 5 shows the position-dependent response of the detector system and how this is manifested in the energy spectrum for ^{99m}Tc . It demonstrates that the energy-tailing is caused by both the depth-dependence and the lateral edges of the CIE map. In principle, there could thus be several CIE maps with different combinations of depth-dependence and lateral shape that would have produced a given spectrum. Figures 2 and 5 demonstrate that collimators with one-to-one anode-hole matching give a consistent shielding of the gaps around all anodes, which affects the low-energy tails of the energy spectra. The matched collimators of the hand-held camera have thus provided valuable information for the model tuning, as the lateral edges of the CIE map are shielded to a varying degree. The use of several radionuclides with different emission energies (and thus different interaction-distributions depth-wise) has similarly provided information for the model. Having access to several matched collimators has likely been the most valuable factor for the model tuning, as this has resulted in drastic changes in the interaction distributions near important regions of the CIE map.

Figures 6 and 7 demonstrate how the model can be used to better understand the detector system and the energy spectrum for ^{177}Lu . Figure 6 concerns comparison of both energy spectra and images, while Fig. 7 shows count rates in energy windows set over the three photopeaks and as a function of source-collimator distance. The distance-dependence is of relevance for practical measurements as the depths of different objects generally vary. From the simulations it is seen that the component causing this distance-dependence is mainly collimator penetration of 208 keV photons, which, owing to the low-energy tail of the CZT detector, affects the count rate not only in the 208 keV window, but also in energy windows set at lower energies. Thus, for any quantitative measurement, this distance-dependence would need to be taken into account.

The CZT model has been valuable for understanding the general behaviour of the hand-held camera. In the future, it may help optimise the use of the camera, including the processing of images. For instance, the possibility to separate the different spectral

contributions based on the original photon energy and interaction history (Fig. 7) provides a tool for development and evaluation of scatter-correction methods that can account for energy-tailing, see e.g. Kacperski et al. [10].

Our future aims include evaluation and application of the model for large-FOV CZT cameras. However, for this stage of model development, the availability of several collimators and list mode data proved to be essential for detailed model tuning and evaluation, and the compact system was found to be very useful as an experimental system.

Conclusion

A CZT detector model has been developed and tuned to closely reflect the response of a CZT-based gamma camera. The model is based on a pre-computed numerical solution to the three-dimensional charge-transport and signal-induction equations, which is coupled to the photon-transport of the SIMIND Monte Carlo program. Model evaluation is made against measured energy spectra and images across several radionuclides and collimators, with good agreements obtained. The model provides insight to the behaviour of the camera system, particularly regarding ^{177}Lu measurements, and will be useful for future optimisation of the camera application.

Abbreviations

CZT: Cadmium zinc telluride; FOV: Field of view; LEHR: Low energy high resolution; MEGP: Medium energy general purpose; FWHM: Full width at half maximum; MCA: Multichannel analyzer; CIE: Charge induction efficiency; SPECT: Single-photon emission computed tomography.

Supplementary Information

The online version contains supplementary material available at <https://doi.org/10.1186/s40658-022-00463-1>.

Additional file 1. Appendix A: provides a more thorough overview of the charge transport and signal induction theories. **Appendix B** describes the inverse-distance-weighted approach to defining the weighting potential on the anode-side of the detector crystal. **Appendix C** describes the energy-calibration procedure. **Appendix D** presents the results of the model tuning for each configuration, and provides an example of the results for one configuration with poorer agreements. **Appendix E** summarises the tunable parameters available under each configuration.

Acknowledgements

The authors wish to acknowledge Dr. Daniel Förnvik, Department of Radiation Physics, Skåne University Hospital, Lund, Sweden, for initial studies of the collimators used.

Author contributions

All authors participated in the experiment design, data analysis, manuscript planning and manuscript editing. DR implemented the signal generation code, implemented the detector model, carried out the experimental measurements and simulations, and wrote the first manuscript draft. ML implemented new features in the SIMIND program necessary for the study. KSG contributed to the first manuscript draft. All authors read and approved the final manuscript.

Funding

Open access funding provided by Lund University. This work was partially funded by the Swedish Cancer Society (Contracts 180747 and 21-1754-Pj01H) and Mrs. Berta Kamprad's Foundation (BKS-2020-13-293).

Availability of data and materials

The datasets used and analysed during the current study are available from the corresponding author on reasonable request. The developed CZT model will be incorporated in a future release of SIMIND (homepage: <https://simind.blogg.lu.se/>).

Declarations

Ethics approval and consent to participate

Not applicable.

Consent for publication

Not applicable.

Competing interests

KSG and MLj received project funding from Fusion Pharmaceuticals Inc., Canada. DR and EL declare that they have nothing to disclose.

Author details

¹Medical Radiation Physics, Lund, Lund University, Lund, Sweden. ²Department of Radiation Physics, Skåne University Hospital, Lund, Sweden.

Received: 12 January 2022 Accepted: 20 April 2022

Published online: 08 May 2022

References

1. Bocher M, Bleviss IM, Tsukerman L, Shrem Y, Kovalski G, Volokh L. A fast cardiac gamma camera with dynamic SPECT capabilities: design, system validation and future potential. *Eur J Nucl Med Mol Imaging*. 2010;37(10):1887–902. <https://doi.org/10.1007/s00259-010-1488-z>.
2. Gambhir SS, Berman DS, Ziffer J, Nagler M, Sandler M, Patton J, Hutton B, Sharir T, Haim SB, Haim SB. A novel high-sensitivity rapid-acquisition single-photon cardiac imaging camera. *J Nucl Med*. 2009;50(4):635–43. <https://doi.org/10.2967/jnumed.108.060020>.
3. Knoll P, Mirzaei S, Schwenkenbecher K, Barthel T. Performance evaluation of a solid-state detector based handheld gamma camera system. *Front Biomed Technol*. 2015;1(1):61–7.
4. Kennedy JA, Reizberg I, Lugassi R, Himmelman S, Keidar Z. Absolute radiotracer concentration measurement using whole-body solid-state SPECT/CT technology: in vivo/in vitro validation. *Med Biol Eng Comput*. 2019;57(7):1581–90.
5. Ito T, Matsusaka Y, Onoguchi M, Ichikawa H, Okuda K, Shibutani T, Shishido M, Sato K. Experimental evaluation of the GE NM/CT 870 CZT clinical SPECT system equipped with WEHR and MEHRS collimator. *J Appl Clin Med Phys*. 2021;22(2):165–77. <https://doi.org/10.1002/acm2.13158>.
6. Desmots C, Bouthiba MA, Enilorac B, Nganoa C, Agostini D, Aide N. Evaluation of a new multipurpose whole-body CZT-based camera: comparison with a dual-head Anger camera and first clinical images. *EJNMMI Phys*. 2020;7(1):18. <https://doi.org/10.1186/s40658-020-0284-5>.
7. Le Rouzig G, Zananiri R. First performance measurements of a new multi-detector CZT-based SPECT/CT system: GE StarGuide. *J Nucl Med*. 2021;62(supplement 1):1125–1125.
8. Owens A, Peacock A. Compound semiconductor radiation detectors. *Nucl Instrum Methods Phys Res Sect A*. 2004;531(1):18–37.
9. Barrett HH, Eskin JD, Barber HB. Charge transport in arrays of semiconductor gamma-ray detectors. *Phys Rev Lett*. 1995;75:156–9.
10. Kacperski K, Erlandsson K, Ben-Haim S, Hutton BF. Iterative deconvolution of simultaneous 99mTc and 201Tl projection data measured on a CdZnTe-based cardiac SPECT scanner. *Phys Med Biol*. 2011;56(5):1397–414.
11. Roth D, Larsson E, Sundlöv A, Sjögreen Gleisner K. Characterisation of a hand-held CZT-based gamma camera for 177Lu imaging. *EJNMMI Phys*. 2020;7(1):46. <https://doi.org/10.1186/s40658-020-00313-y>.
12. Strosberg J, El-Haddad G, Wolin E, Hendifar A, Yao J, Chasen B, Mittra E, Kunz PL, Kulke MH, Jacene H, Bushnell D, O'Dorisio TM, Baum RP, Kulkarni HR, Caplin M, Lebtahi R, Hobday T, Delpassand E, Van Cutsem E, Benson A, Srirajaskanthan R, Pavel M, Mora J, Berlin J, Grande E, Reed N, Seregini E, Öberg K, Lopera SM, Santoro P, Thevenet T, Erion JL, Ruzsniowski P, Kwekkeboom D, Krenning E. Phase 3 trial of 177Lu-Dotatate for midgut neuroendocrine tumors. *N Engl J Med*. 2017;376(2):125–35.
13. Fendler WP, Rahbar K, Herrmann K, Kratochwil C, Eiber M. 177Lu-PSMA radioligand therapy for prostate cancer. *J Nucl Med*. 2017;58(8):1196–200.
14. Violet J, Jackson P, Ferdinandus J, Sandhu S, Akhurst T, Iravani A, Kong G, Kumar AR, Thang SP, Eu P, Scalzo M, Murphy D, Williams S, Hicks RJ, Hofman MS. Dosimetry of 177Lu-PSMA-617 in metastatic castration-resistant prostate cancer: correlations between pretherapeutic imaging and whole-body tumor dosimetry with treatment outcomes. *J Nucl Med*. 2019;60(4):517–23.
15. Holstenson M, Erlandsson K, Poludniowski G, Ben-Haim S, Hutton BF. Model-based correction for scatter and tailing effects in simultaneous 99mTc and 123I imaging for a CdZnTe cardiac SPECT camera. *Phys Med Biol*. 2015;60(8):3045–63.
16. Fan P, Hutton BF, Holstenson M, Ljungberg M, Pretorius PH, Prasad R, Ma T, Liu Y, Wang S, Thorn SL, Stacy MR, Sinusas AJ, Liu C. Scatter and crosstalk corrections for 99mTc/123I dual-radionuclide imaging using a CZT SPECT system with pinhole collimators. *Med Phys*. 2015;42(12):6895–911.
17. Takeuchi W, Suzuki A, Shiga T, Kubo N, Morimoto Y, Ueno Y, Kobashi K, Umegaki K, Tamaki N. Simultaneous Tc-99m and I-123 dual-radionuclide imaging with a solid-state detector-based brain-SPECT system and energy-based scatter correction. *EJNMMI Phys*. 2016;3(1):10.
18. Blaire T, Bailliez A, Bouallegue FB, Bellevre D, Agostini D, Manrique A. Left ventricular function assessment using 123I/99mTc dual-isotope acquisition with two semi-conductor cadmium-zinc-telluride (CZT) cameras: a gated cardiac phantom study. *EJNMMI Phys*. 2016;3(1):27. <https://doi.org/10.1186/s40658-016-0163-2>.
19. Prettyman TH. Method for mapping charge pulses in semiconductor radiation detectors. *Nucl Instrum Methods Phys Res Sect A*. 1999;422(1):232–7.
20. Hamel L-A, Paquet S. Charge transport and signal generation in CdTe pixel detectors. *Nucl Instrum Methods Phys Res Sect A*. 1996;380(1):238–40.
21. Myronakis ME, Zvelebil M, Darambara DG. Computational modelling of pixelated CdZnTe detectors for x- and y- ray imaging applications. *J Instrum*. 2012;7(03):P03004–P03004. <https://doi.org/10.1088/1748-0221/7/03/p03004>.
22. Guerra P, Santos A, Darambara DG. Development of a simplified simulation model for performance characterization of a pixelated CdZnTe multimodality imaging system. *Phys Med Biol*. 2008;53(4):1099–113.

23. Pretorius PH, Liu C, Fan P, Peterson M, Ljungberg M. Monte Carlo simulations of the GE Discovery Alcyone CZT SPECT systems. *IEEE Trans Nucl Sci.* 2015;62(3):832–9.
24. Ljungberg M, Strand S-E. A Monte Carlo program for the simulation of scintillation camera characteristics. *Comput Methods Programs Biomed.* 1989;29(4):257–72.
25. Kotoch TB, Nandi A, Debnath D, Malkar JP, Rao AR, Hingar MK, Madhav VP, Sreekumar S, Chakrabarti SK. Instruments of RT-2 experiment onboard CORONAS-PHOTON and their test and evaluation II: RT-2/CZT payload. *Exp Astron.* 2011;29(1):27–54.
26. Shockley W. Currents to conductors induced by a moving point charge. *J Appl Phys.* 1938;9(10):635–6.
27. Ramo S. Currents induced by electron motion. *Proc IRE.* 1939;27(9):584–5.
28. He Z. Review of the Shockley–Ramo theorem and its application in semiconductor gamma-ray detectors. *Nucl Instrum Methods Phys Res Sect A.* 2001;463(1):250–67.
29. Knoll GF. Radiation detection and measurement. 4th ed. Hoboken: Wiley; 2010.
30. Myronakis ME, Darambara DG. Monte Carlo investigation of charge-transport effects on energy resolution and detection efficiency of pixelated CZT detectors for SPECT/PET applications. *Med Phys.* 2011;38(1):455–67.
31. Mathy F, Gliere A, d'Aillon EG, Masse P, Picone M, Tabary J, Verger L. A three-dimensional model of CdZnTe gamma-ray detector and its experimental validation. *IEEE Trans Nucl Sci.* 2004;51(5):2419–26.
32. Einstein A. Über die von der molekularkinetischen theorie der wärme geforderte bewegung von in ruhenden flüssigkeiten suspendierten teilchen. *Ann Phys.* 1905;322(8):549–60. <https://doi.org/10.1002/andp.19053220806>.
33. Vadawale SV, Purohit S, Shanmugam M, Acharya YB, Goswami JN, Sudhakar M, Sreekumar P. Characterization and selection of CZT detector modules for HEX experiment onboard Chandrayaan-1. *Nucl Instrum Methods Phys Res Sect A.* 2009;598(2):485–95.
34. NEMA. NEMA standards publication NU 1-2012: performance measurements of gamma cameras. National Electrical Manufacturers Association, Rosslyn, Virginia, USA. 2013.
35. Oliphant TE. Python for scientific computing. *Comput Sci Eng.* 2007;9(3):10–20.
36. Virtanen P, Gommers R, Oliphant TE, Haberland M, Reddy T, Cournapeau D, Burovski E, Peterson P, Weckesser W, Bright J, van der Walt SJ, Brett M, Wilson J, Jarrod Millman K, Mayorov N, Nelson ARJ, Jones E, Kern R, Larson E, Carey C, Polat I, Feng Y, Moore EW, VanderPlas J, Laxalde D, Perktold J, Cimrman R, Henriksen I, Quintero EA, Harris CR, Archibald AM, Ribeiro AH, Pedregosa F, van Mulbregt P and SciPy 1.0 Contributors. Fundamental algorithms for scientific computing in Python. *SciPy 1.0. Nat Methods.* 2020;17:261–72. <https://doi.org/10.1038/s41592-019-0686-2>.
37. Press WH, Teukolsky SA, Vetterling WT, Flannery BP. Numerical recipes 3rd edition: the art of scientific computing, chapter 20: Partial Differential Equations, p. 1024–1096. Cambridge university press, New York, USA, 2007. ISBN 978-0-521-88068-8.
38. Baker AH, Jessup ER, Manteuffel T. A technique for accelerating the convergence of restarted GMRES. *SIAM J Matrix Anal Appl.* 2005;26(4):962–84.
39. Mardor I, Shor A, Eisen Y. Edge and corner effects on spectra of segmented CdZnTe detectors. *IEEE Trans Nucl Sci.* 2001;48(4):1033–40.
40. Richter RH, Andricek L, Gebhart T, Hauff D, Kemmer J, Lutz G, Weiß R, Rolf A. Strip detector design for ATLAS and HERA-B using two-dimensional device simulation. *Nucl Instrum Methods Phys Res Sect A Accelerat Spectrom Detect Assoc Equip.* 1996;377(2):412–21. ISSN 0168-9002. Proceedings of the Seventh European Symposium on Semiconductor.
41. Bolotnikov AE, Cook WR, Harrison FA, Wong AS, Schindler SM, Eichelberger AC. Charge loss between contacts of CdZnTe pixel detectors. *Nucl Instrum Methods Phys Res Sect A.* 1999;432(2):326–31.
42. Prettyman TH, Ameduri FP, Burger A, Gregory JC, Hoffbauer MA, Majerus PR, Reisenfeld DB, Soldner SE, Sezeles C. Effect of surfaces on the performance of CdZnTe detectors. In: James Ralph B, editor. *Hard X-ray and gamma-ray detector physics III.* volume 4507. SPIE: International Society for Optics and Photonics; 2001. p. 23–31.
43. Tousignant O, Hamel LA, Vasilevski D. Weighting potentials in CdZnTe γ -ray detectors with segmented electrodes. *IEEE Trans Nucl Sci.* 2000;47(6):2084–6.
44. d'Aillon EG, Gentet MC, Montemont G, Rustique J, Verger L. Simulation and experimental results on monolithic CdZnTe gamma-ray detectors. *IEEE Trans Nucl Sci.* 2005;52(6):3096–102.
45. Shepard D. A two-dimensional interpolation function for irregularly-spaced data. In: Proceedings of the 1968 23rd ACM national conference, ACM'68, p. 517–524, New York, NY, USA, 1968. Association for Computing Machinery. ISBN 9781450374866.
46. Xu C, Danielsson M, Bornefalk H. Evaluation of energy loss and charge sharing in cadmium telluride detectors for photon-counting computed tomography. *IEEE Trans Nucl Sci.* 2011;58(3):614–25.
47. Park HR, Youn H, Han JC, Kam SH, Kim HK. Finite element analysis of the effects of pixel geometry on the electrical properties in semiconductor pixel detectors. *J Korean Phys Soc.* 2013;62(5):813–9.
48. Hecht K. Zum mechanismus des lichtelektrischen primärstromes in isolierenden kristallen. *Z Phys.* 1932;77(3):235–45.
49. Vassiliev ON. Monte Carlo methods for radiation transport: fundamentals and advanced topics, chapter 4: particle trajectories, tallies, and variance reduction, p. 105–39. Springer International Publishing, Cham, Switzerland, 2017. ISBN 978-3-319-44141-2.
50. d'Aillon EG, Tabary J, Glière A, Verger L. Charge sharing on monolithic CdZnTe gamma-ray detectors: a simulation study. *Nucl Instrum Methods Phys Res Sect A Accelerat Spectrom Detect Assoc Equip.* 2006;563(1):124–7. ISSN 0168-9002. Proceedings of the 7th International Workshop on Radiation Imaging Detectors.
51. James RB, Brunett B, Heffelfinger J, Van Scyoc J, Lund J, Doty FP, Lingren CL, Olsen R, Cross E, Hermon H, Yoon H, Hilton N, Schieber M, Lee EY, Toney J, Schlesinger TE, Goorsky M, Yao W, Chen H, Burger A. Material properties of large-volume cadmium zinc telluride crystals and their relationship to nuclear detector performance. *J Electron Mater.* 1998;27(6):788–99.
52. Mayer M, Boykin DV, Cherry ML, Courville JF, Doty FP, Drake A, Guzik TG, Hamel LA, Larson K, Macri JR, McConnell ML, Ryan JM, Tousignant O. Performance and simulation of CdZnTe strip detectors as sub-millimeter resolution imaging gamma radiation spectrometers. *IEEE Trans Nucl Sci.* 1997;44(3):922–8.

53. McGregor DS, Hermon H. Room-temperature compound semiconductor radiation detectors. *Nucl Instrum Methods Phys Res Sect A*. 1997;395(1):101–24.
54. Bolotnikov AE, Camarda GC, Wright GW, James RB. Factors limiting the performance of CdZnTe detectors. *IEEE Trans Nucl Sci*. 2005;52(3):589–98.
55. Nelder JA, Mead R. A simplex method for function minimization. *Comput J*. 1965;7(4):308–13.
56. Jung I, Krawczynski H, Komarov S, Sobotka L. Simulation studies of CZT detectors as gamma-ray calorimeter. *Astropart Phys*. 2006;26(2):119–28. <https://doi.org/10.1016/j.astropartphys.2006.05.009>.
57. Berger MJ, Coursey JS, Zucker MA, Chang J. ESTAR, PSTAR, and ASTAR: computer programs for calculating stopping-power and range tables for electrons, protons, and helium ions (version 2.0.1). <http://physics.nist.gov/Star> [2020-11-12], 2017. National Institute of Standards and Technology, Gaithersburg, MD.
58. Gustafsson J, Brolin G, Ljungberg M. Monte Carlo-based SPECT reconstruction within the SIMIND framework. *Phys Med Biol*. 2018;63(24): 245012. <https://doi.org/10.1088/1361-6560/aaf0f1>.

Publisher's Note

Springer Nature remains neutral with regard to jurisdictional claims in published maps and institutional affiliations.

Submit your manuscript to a SpringerOpen[®] journal and benefit from:

- ▶ Convenient online submission
- ▶ Rigorous peer review
- ▶ Open access: articles freely available online
- ▶ High visibility within the field
- ▶ Retaining the copyright to your article

Submit your next manuscript at ▶ [springeropen.com](https://www.springeropen.com)
